SvedbergOpen
DISSEMINATION OF KNOWLEDGE

International Journal of Artificial Intelligence and Machine Learning

Publisher's Home Page: https://www.svedbergopen.com/

Research Paper Open Access

A Detailed Investigation of A 10 Ghz X-Band 4×7 Tapered Series-Fed Microstrip Patch Array for Radar Applications

Kadire.Sumalatha[1], Dr. Pradeep Vinaik Kodavanti[2]

[1]*Research Scholar, Department of EECE, GITAM (Deemed to be University), Visakhapatnam-530045, Andhra Pradesh, India
[2]Assistant Professor, Department of EECE, GITAM (Deemed to be University), Visakhapatnam-530045, Andhra Pradesh, India
*Corresponding Author Email: kadire.suma@gmail.com

ABSTRACT

This paper presents a detailed design, full-wave simulation, fabrication, and experimental evaluation of a vertically polarized 4 × 7 series-fed microstrip patch antenna array intended for X-band radar operation around 10 GHz. The array contains 28 printed radiating elements arranged as four series-fed branches with seven patches per branch. The prototype is implemented on Rogers RT/duroid 5880 having a relative dielectric constant of 2.2 and a substrate thickness of 0.8 mm. A nonuniform, linearly tapered patch distribution is used in the array geometry to shape the aperture excitation and reduce the sidelobe level while preserving a simple low-profile printed structure. The antenna is modeled in Ansys HFSS and subsequently fabricated for experimental validation. The reported simulation results show a peak gain of approximately 19 dBi, a half-power beamwidth of approximately 18°, a sidelobe level about 12 dB below the main beam, and a fixed beam tilt of approximately 20°. Impedance matching is evaluated using S11 and VSWR. After fabrication, copper tuning stubs are added to the feed-divider tracks to improve the measured input match. Vector-network-analyzer measurements show a response that follows the simulated trend, while chamber measurements reported in the source indicate that the measured gain remains within approximately 0.5–1 dB of the simulated gain across the operating band. The study demonstrates the practical feasibility of a compact printed series-fed array for directional X-band radar and target-tracking applications. The paper also clarifies the relationship between element spacing, feed-line phase progression, and fixed beam tilt, and identifies measurement quantities that should be reported in future work for stronger quantitative validation.

Keywords—X-band radar, microstrip patch antenna, 4 × 7 array, series-fed array, tapered aperture, vertical polarization, HFSS, sidelobe suppression, beam tilt, antenna measurement.

1. Introduction

X-band radar systems are widely used for target detection, tracking, surveillance, navigation, and remote-sensing applications, where antenna gain, beamwidth, sidelobe level, polarization, and impedance matching strongly influence the overall system performance. For directional radar operation, the antenna is required to concentrate electromagnetic energy within a narrow angular region while maintaining adequate gain and controlled sidelobe radiation. Conventional array technologies can provide high directivity and polarization diversity; however, their structural complexity, feeding requirements, and physical size can increase the difficulty of integration with compact radar front ends. X-band array antennas have therefore received considerable attention for applications requiring directional radiation characteristics and practical planar implementation [1]-[4]. Microstrip patch antennas provide an attractive platform for such applications because the radiating elements and feeding structures can be fabricated on a common dielectric substrate using established printed-circuit techniques. Their low profile, relatively low weight, and compatibility with microwave circuits make them suitable for compact radar and remote-sensing systems. Previous investigations have demonstrated different microstrip configurations, including aperture-coupled, stacked, dual-polarized, and dual-band structures, to improve bandwidth, isolation, polarization characteristics, and radiation performance [5]-[8]. However, a single patch generally provides limited directivity and gain; consequently, multiple patches must be combined into an array to obtain a larger effective aperture and a more directional radiation pattern.

The performance of a microstrip array depends strongly on the selected feeding topology. Corporate-fed arrays provide direct control over the amplitude and phase excitation of individual elements but require a relatively extensive network of power dividers and transmission lines. In contrast, a series-fed configuration connects radiating elements sequentially along a transmission path, reducing feed-network complexity and potentially providing a more compact implementation. Earlier investigations of dual-polarized and integrated microstrip arrays established the importance of feed architecture, element interaction, and phase control in achieving the desired radiation characteristics [9], [10], [11], while previous work on integrated feeding and polarization architectures further demonstrated the potential of printed feed networks for radaroriented arrays [12]. In particular, series-fed microstrip arrays operating around 10 GHz have demonstrated the suitability of sequential feeding for achieving directional radiation with a relatively simple planar structure [13].

An important challenge in series-fed arrays is the simultaneous control of excitation amplitude and phase along the radiating aperture. As the electromagnetic signal propagates from one patch to the next, the available power decreases and the accumulated electrical phase changes according to the transmission-line geometry. Consequently, the dimensions of individual patches, inter-element spacing, and feed-line lengths directly affect the resulting radiation pattern. Nonuniform aperture excitation can be introduced to reduce sidelobe radiation, while appropriate phase progression can determine the direction of the principal beam. Recent X-band array investigations have demonstrated that carefully designed planar feeding networks can provide high gain, narrow beams, and controlled sidelobe characteristics without requiring electronically controlled phase shifters [14]-[16]. These studies indicate that feed-network design and aperture excitation should be considered simultaneously rather than treating the radiating patches as isolated elements.

Sidelobe suppression is particularly important in radar systems because excessive sidelobe radiation can increase the response to unwanted targets, clutter, and interference. Amplitude tapering is therefore commonly employed to reduce the excitation of elements toward the aperture edges and obtain a more favorable radiation distribution. Recent studies have investigated tapered series-fed patch arrays, traveling-wave feeding, and other nonuniform excitation techniques for achieving reduced sidelobe levels while maintaining useful gain and bandwidth [17]-[20]. A series-fed array using a traveling-wave configuration can exploit the progressive excitation of the elements, whereas other approaches employ optimized feed networks or controlled excitation distributions to obtain lower sidelobes. These developments demonstrate that sidelobe performance is closely associated with the relationship between the physical aperture distribution and the electrical phase progression. Recent research has also explored more advanced approaches for improving the gain, bandwidth, efficiency, and radiation characteristics of printed X-band arrays. Compact series-fed arrays have been investigated using modified transmission-line structures and optimized excitation distributions [21]. Metasurface and artificial electromagnetic structures have also been incorporated into microstrip arrays to enhance gain and modify the radiation pattern [22]. Other recent X-band antenna developments have considered compact printed structures for specialized radar and search-and-rescue applications, as well as frequency-selective surfaces for gain enhancement and multiband operation [23], [24]. Although such techniques can provide significant electromagnetic improvements, they may introduce additional layers, fabrication steps, electromagnetic structures, or optimization requirements. Consequently, there remains a practical need for relatively simple single-layer series-fed arrays that can provide a suitable compromise among gain, beamwidth, sidelobe level, impedance matching, fabrication complexity, and experimental realizability.

Recent engineering research by the authors has additionally investigated intelligent control, adaptive optimization, experimentally validated hardware, and integrated energy-conversion systems, including fuzzy-based power-converter control, AI-enabled multi-objective infrastructure planning, resilient multi-agent energy management, switched-capacitor power conversion, digital-twin-enabled reinforcement learning, integrated solar-PV motor-drive control, and learning-assisted adaptive power-flow control [25]-[28]. Although these studies are primarily concerned with electric mobility, renewable-energy systems, power electronics, and intelligent control rather than antenna design, they demonstrate a broader research direction toward combining physical hardware with intelligent modeling, optimization, adaptive control, and experimental validation. Such system-level considerations are increasingly relevant to future radar platforms in which sensing, RF hardware, signal processing, power conversion, and intelligent decision-making are integrated within compact systems. The present antenna study complements this broader research direction by emphasizing a physically realizable RF aperture together with full-wave electromagnetic analysis, prototype fabrication, and experimental characterization.

Motivated by these considerations, this work presents a detailed investigation of a 10 GHz, 4 × 7 tapered series-fed microstrip patch array comprising 28 vertically polarized radiating elements for directional X-band radar applications. The proposed structure combines a printed input divider with four series-fed branches, while nonuniform patch dimensions are employed to shape the aperture excitation and control sidelobe radiation. The antenna is implemented on Rogers RT/duroid 5880 with a relative dielectric constant of 2.2 and substrate thickness of 0.8 mm. The complete structure is modeled using Ansys HFSS, followed by prototype fabrication, vector-network-analyzer measurements, and anechoic-chamber radiation characterization. The reported simulation results provide approximately 19 dBi peak gain, 18° half-power beamwidth, a sidelobe level approximately 12 dB below the principal beam, and a fixed beam tilt of approximately 20°. The experimental investigation further examines the impedance response and the effect of copper tuning stubs introduced in the feed-divider tracks to compensate for fabrication-related deviations. The relationship between element spacing, feed-line electrical length, aperture tapering, phase progression, and fixed beam direction is consequently analyzed. Unlike electronically scanned arrays, the demonstrated structure employs a passive feed configuration and therefore provides a fixed directional beam rather than electronic beam steering. The resulting design provides a practical experimentally validated approach for compact X-band radar arrays where high directivity, controlled sidelobes, and relatively simple printed fabrication are required [29], [30].

The main technical objectives of the reported design can be summarized as follows:

- to realize a 10 GHz, 28-element printed microstrip array suitable for directional X-band radar operation;
- to use a simple series-fed architecture combined with a corporate input divider;
- to taper the patch dimensions to control the aperture distribution and suppress sidelobes;
- to obtain a high directional gain and a narrow principal beam with a fixed beam tilt;
- to compare the HFSS impedance and radiation predictions with fabricated-hardware measurements; and
- to demonstrate practical post-fabrication impedance tuning using copper stubs on the feed network.

2. ANTENNA CONFIGURATION AND PHYSICAL DESIGN

2.1 Array Topology

The proposed antenna consists of 28 rectangular microstrip patches arranged in a 4 × 7 configuration. The four vertical branches are fed from a common input through a printed divider network, while the seven radiating elements in each branch are connected in series. This arrangement combines a corporate distribution stage at the array input with series-fed radiating branches. The resulting layout is compact and avoids the extensive routing that would be required if a separate corporate feed were taken to each of the 28 radiators.

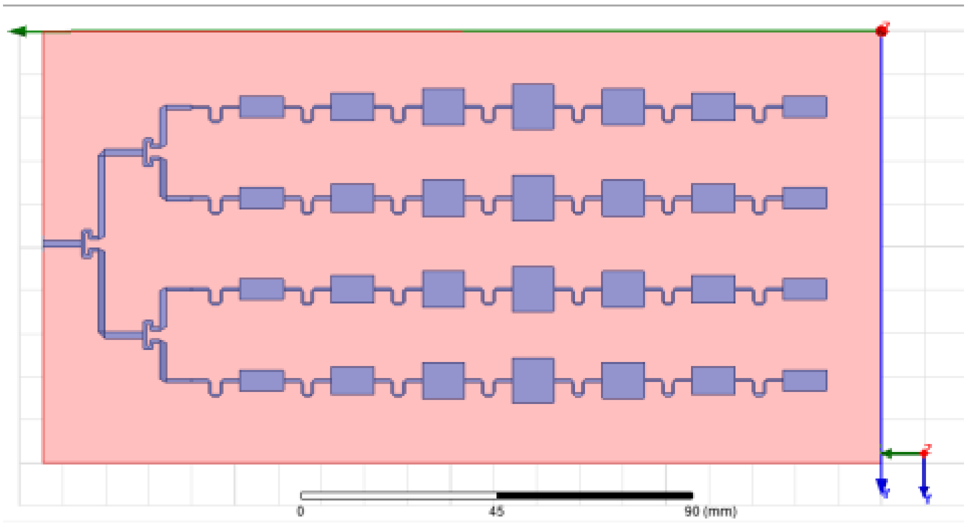

Fig. 1. HFSS top view of the 4 × 7 series-fed patch array and the printed input feed-divider section.

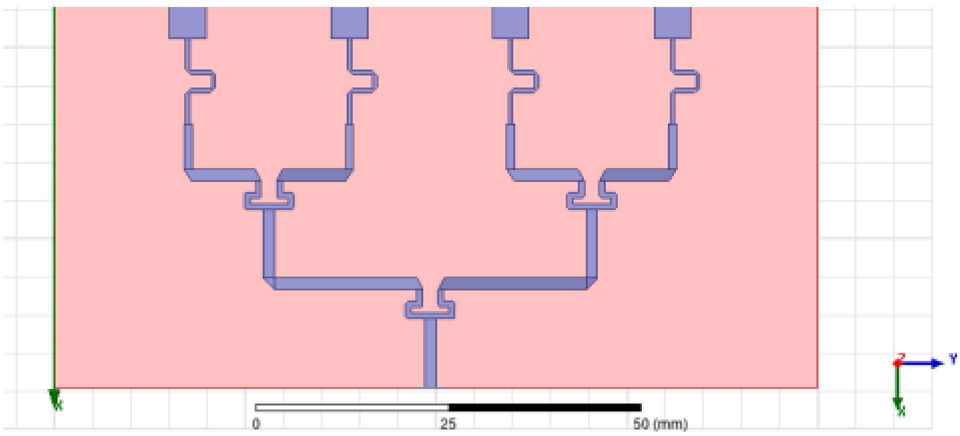

Fig. 2. Enlarged view of the lower feed-divider region that distributes the input signal to the four series-fed branches

The four columns in Fig. 1 are visually symmetric about the center of the array. The lower feed section splits the input path into the four radiating branches. Because each branch contains a chain of patches and interconnecting transmission-line sections, the input signal experiences both amplitude reduction and phase progression as it travels through the branch. The geometry of each successive patch therefore contributes to the final aperture distribution.

Table I. Summary of Reported Design and Performance Parameters

Parameter	Reported / Derived Value
Center/design frequency	10 GHz
Array configuration	4 × 7 = 28 elements
Polarization	Vertical
Substrate	Rogers RT/duroid 5880
Relative permittivity, εr	2.2
Substrate thickness, h	0.8 mm
Overall array dimension	Approximately 185 mm × 100 mm as stated in the manuscript
Element spacing	0.75λ stated in the manuscript; direction-specific spacing should be explicitly documented
Simulated peak gain	Approximately 19 dBi
Simulated HPBW	Approximately 18°
Reported sidelobe level	About 12 dB below the main beam
Reported beam tilt	Approximately 20°
Measurement methods	VNA and anechoic-chamber testing
Post-fabrication tuning	Copper stubs added to the feed-divider tracks
Gain agreement	Measured and simulated values reported within approximately 0.5–1 dB

2.2 Substrate and Fabricated Geometry

The radiating structure is fabricated on Rogers RT/duroid 5880. The relative dielectric constant reported for the substrate is εr = 2.2 and the substrate thickness is h = 0.8 mm. A low dielectric constant is beneficial for microstrip radiation because it supports fringing fields and reduces the degree of field confinement compared with a high-permittivity substrate. The selected laminate is also widely used for microwave printed structures where stable dielectric properties are required.

Fig. 3. Fabricated 4 × 7 microstrip patch array on the Rogers 5880 laminate.

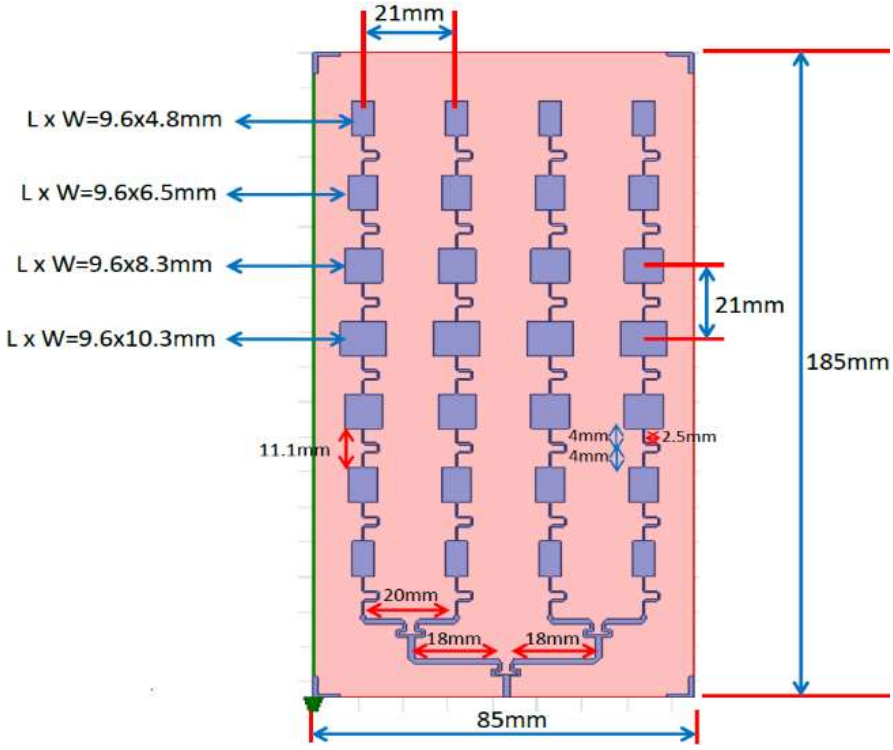

Fig. 4. Dimensioned array drawing included in the source manuscript. The figure should be treated as the primary geometry reference where individual values are legible.

The source manuscript states an assembled array dimension of approximately 185 mm × 100 mm. The dimensioned drawing provides additional local dimensions, but the source does not provide a complete tabulation of every patch width, patch length, inter-element line length, feed-line width, and taper value. For reproducibility, a future submission should include a complete geometry table rather than relying only on the image.

2.3 Element Spacing and Aperture Tapering

The manuscript states that the spacing between antenna elements is 0.75λ. At 10 GHz, the free-space wavelength is 30 mm, so a spacing of 0.75λ corresponds to 22.5 mm. The phase response of a series-fed branch depends on the relevant physical separation and transmission-line electrical length. Because the layout contains both vertical spacing along a branch and horizontal spacing between branches, the final manuscript should identify the spacing value separately for each array axis. This is particularly important when relating the feed geometry to the reported 20° beam tilt.

The patch dimensions shown in the array are tapered rather than uniform. In an array, amplitude tapering is commonly used to reduce sidelobes by lowering the excitation of elements near the aperture edges relative to the central region. In this design, the intended taper is implemented through the patch and series-feed geometry rather than through a separate attenuator network. The reported simulation shows a sidelobe level approximately 12 dB below the main beam. The source, however, does not give a complete numerical list of the excitation coefficients or the individual patch dimensions, so the exact taper law cannot be reconstructed solely from the text.

3. DESIGN EQUATIONS AND CALCULATIONS

The initial dimensions of the rectangular patch elements can be estimated using standard microstrip-patch expressions. The following equations present the intended design relationships in a complete form. They clarify formulae that were incomplete in the source draft and do not introduce additional measured data.

3.1 Patch Width

For a rectangular microstrip patch designed around a resonant frequency f0, an initial estimate of the patch width W is

$$W = (c / 2f_0) \sqrt{[2 / (\varepsilon_r + 1)]} \qquad (1)$$

where c is the speed of light in free space, f0 is the design frequency, and εr is the relative dielectric constant of the substrate. The patch width influences the input impedance, radiation conductance, and fringing-field distribution.

3.2 Effective Dielectric Constant

Because part of the microstrip field propagates in the dielectric and part propagates in air, the patch can be described using an effective relative permittivity εeff. A commonly used approximation is

$$\varepsilon eff = (\varepsilon_r + 1)/2 + (\varepsilon_r - 1)/2 \cdot [1 + 12h/W]^{-1/2} \quad (2)$$

The effective dielectric constant is lower than the substrate dielectric constant because the fringing fields extend into the air region above the substrate.

3.3 Effective Length and Fringing-Length Extension

For the dominant rectangular-patch mode, the effective resonant length is approximated by

$$Leff = c / [2f_0\sqrt{\varepsilon eff}] \quad (3)$$

The physical patch is shorter than Leff because the fringing fields effectively extend the resonant length beyond the metallized edge. The normalized length extension can be estimated as

$$\Delta L/h = 0.412 \cdot [(\varepsilon eff + 0.3)(W/h + 0.264)] / [(\varepsilon eff - 0.258)(W/h + 0.8)] \quad (4)$$

and the physical patch length L is then

$$L = Leff - 2\Delta L \quad (5)$$

3.4 Ground-Plane Estimate

The source manuscript uses the conventional first-order estimate

$$Lg = L + 6h, \quad Wg = W + 6h \quad (6)$$

for the minimum local ground-plane dimensions around an isolated patch. In the present array, however, the radiators share a larger common substrate and ground plane, so the overall PCB dimensions are determined by the complete array aperture and feed layout rather than by the isolated-element estimate alone.

3.5 Guided Wavelength and Electrical Length

The phase accumulated in a printed feed section depends on the guided wavelength rather than the free-space wavelength. A first-order microstrip approximation is

$$\lambda g \approx \lambda_0 / \sqrt{\varepsilon eff} \quad (7)$$

$$\beta = 2\pi / \lambda g \quad (8)$$

$$\theta e = \beta \ell \quad (9)$$

where λ0 is the free-space wavelength, β is the propagation constant, ℓ is the physical transmission-line length, and θe is the corresponding electrical phase length. In a series-fed array, small changes in inter-element line length can therefore shift the main beam and alter the impedance response.

3.6 Feed-Line Impedance

The source manuscript indicates that 50 Ω, 70 Ω, and 100 Ω microstrip sections were considered in the feed network. The required line widths depend on εr, substrate thickness h, conductor thickness t, and the effective permittivity. For a final reproducible design, the exact widths of each impedance section should be stated numerically in a geometry table. The source figures confirm the use of multiple printed line widths, but the complete numerical values are not available in the manuscript text.

3.7 Array-Gain Estimate

A simple upper-bound estimate for the gain improvement from N identical coherently excited elements is

$$Garray \approx Gi + 10\log_{10}(N) \quad (10)$$

For N = 28 and a stated individual-element gain of approximately Gi = 6 dBi, the idealized estimate is

$$Garray \approx 6 + 10\log_{10}(28) = 20.47 \text{ dBi} \quad (11)$$

The HFSS result is approximately 19 dBi. This difference is physically reasonable because the idealized expression does not include nonuniform taper, feed-network loss, conductor and dielectric loss, mutual coupling, impedance mismatch, finite radiation efficiency, and the fact that the isolated-element gain does not necessarily remain unchanged when the elements are embedded in the complete array.

Table II. Basic Calculated Values at 10 Ghz

Quantity	Calculation	Value
Free-space wavelength, λ0	c/f	30 mm
0.5λ0 spacing	0.5 × 30 mm	15 mm
0.75λ0 spacing	0.75 × 30 mm	22.5 mm
Ideal 28-element gain increment	10log10(28)	14.47 dB
Idealized gain with Gi = 6 dBi	6 + 14.47	20.47 dBi
HFSS peak gain	Reported simulation result	≈ 19 dBi

4. HFSS MODELING AND SIMULATION PROCEDURE

4.1 Electromagnetic Model

The complete 4 × 7 antenna was modeled in Ansys HFSS, version 19 as stated in the figure caption of the source manuscript. The simulation includes the 28 printed patches, the inter-element series-feed lines, the lower feed-divider region, the dielectric substrate, and the ground structure. Full-wave simulation is necessary because the 28-element array cannot be accurately described by isolated-patch formulas alone;

mutual coupling, discontinuities, finite substrate size, and the distributed phase of the feed network all influence the final impedance and radiation characteristics.

The source manuscript does not specify the HFSS port definition, radiation-boundary distance, adaptive-mesh convergence criterion, frequency-sweep type, or final mesh density. These settings affect reproducibility and should be documented in a future submission. The results presented here therefore describe the reported outputs of the HFSS model without inventing unreported solver settings.

4.2 Simulated Quantities

The simulation was used to evaluate the input reflection coefficient S11, VSWR, three-dimensional gain, and two-dimensional radiation patterns. These quantities were selected because they characterize both the impedance compatibility of the antenna with a nominal 50 Ω feed and the directional radiation performance required for radar operation. The simulated patterns were also used to identify the main-beam direction, half-power beamwidth, and sidelobe level.

5. SIMULATION RESULTS AND ANALYSIS

5.1 Three-Dimensional Gain

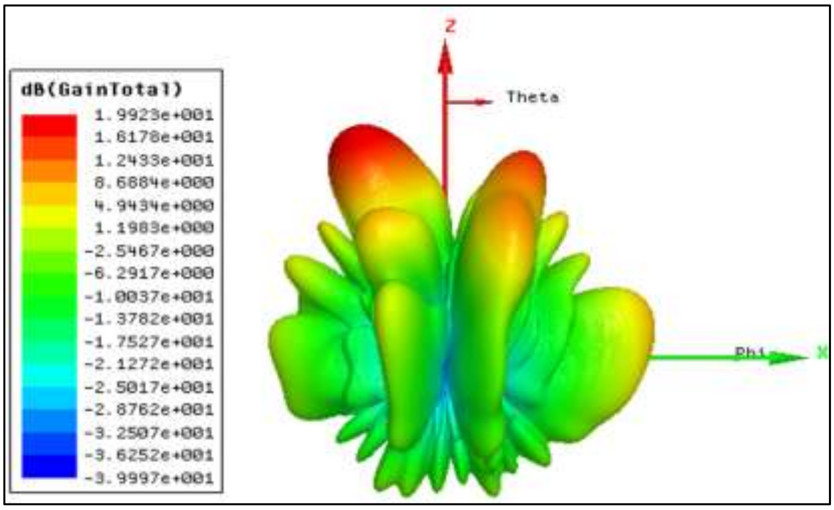

Fig. 5. Simulated three-dimensional gain pattern. The reported peak gain is approximately 19 dBi.

Figure 5 shows the simulated three-dimensional radiation pattern. The maximum reported gain is approximately 19 dBi. The pattern is strongly directional, which is consistent with the large electrical aperture produced by the 28-element arrangement. The multiple lower-level lobes visible away from the principal beam are expected in a finite array, and their magnitude is influenced by the element spacing, amplitude taper, mutual coupling, and phase progression along the feed network.

5.2 Principal-Plane Radiation Pattern

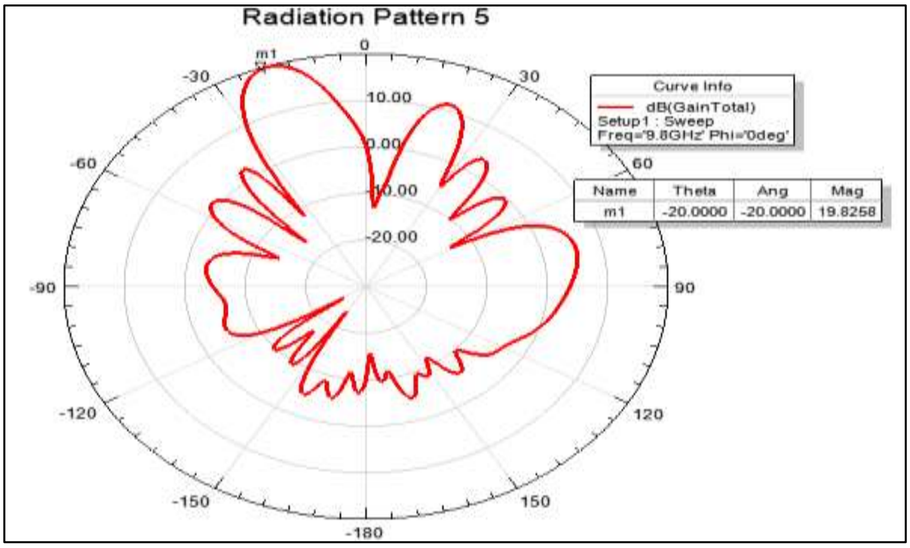

Fig. 6. Simulated polar radiation pattern showing the principal lobe and sidelobe structure

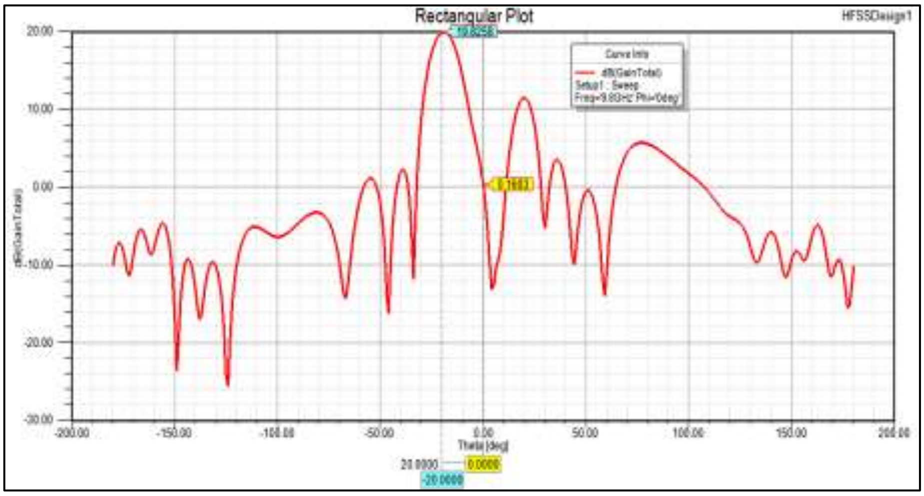

Fig. 7. Rectangular representation of the simulated radiation pattern used to estimate beamwidth and beam tilt.

The source manuscript reports a half-power beamwidth (HPBW) of approximately 18°, a sidelobe level about 12 dB below the principal maximum, and a beam tilt of approximately 20°. A narrow HPBW is desirable in radar because it improves angular selectivity and concentrates the radiated energy into a smaller angular sector. The 20° beam tilt indicates that the direction of maximum radiation is displaced from broadside. In a passive series-fed array, such a fixed tilt is produced by the progressive phase accumulated through the feed-line sections and by the element spacing; it is not evidence of electronically reconfigurable steering.

The original text refers to H-plane and E-plane patterns, while the available figure captions both describe an azimuth-type view. For a publication-ready version, the measurement and simulation coordinate system should be explicitly defined, and the E-plane and H-plane plots should be separately labeled with φ and θ cuts. This would remove ambiguity concerning the plane in which the 18° HPBW and 20° tilt were measured.

5.3 Simulated Reflection Coefficient

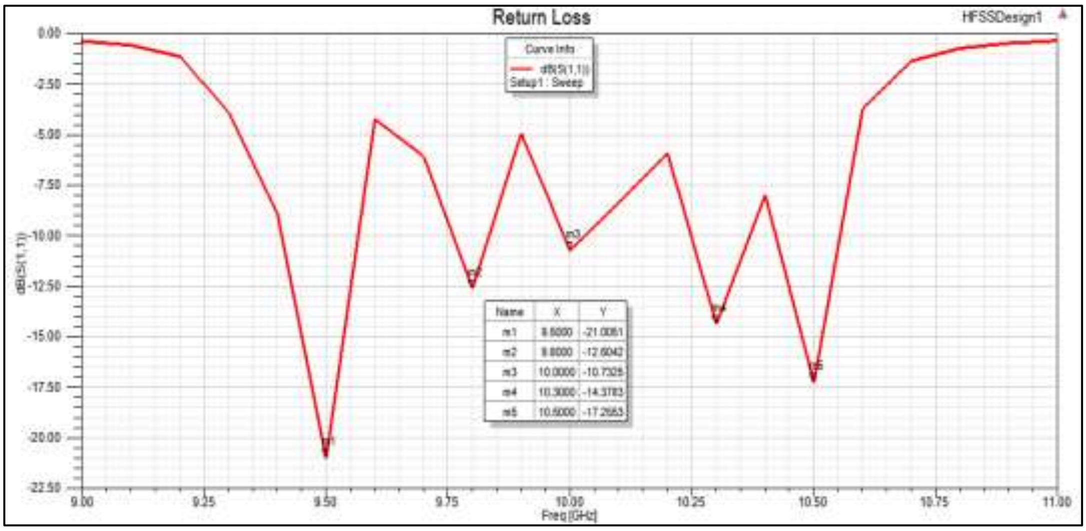

Fig. 8. HFSS-simulated S11 response for the vertically polarized antenna array

Figure 8 shows the simulated input reflection coefficient. The plot contains several resonant features rather than a single isolated resonance. This behavior is consistent with a multi-element series-fed structure in which the radiating patches and feed-line discontinuities interact over frequency. The design objective is to maintain sufficiently low |S11| over the intended operating region. When S11 is expressed in dB, a common matching criterion is S11 ≤ −10 dB, which corresponds to a return loss of at least 10 dB.

The source manuscript states that the return loss is better than approximately 12 dB in the required band, but it does not provide the exact lower and upper −10 dB frequencies in numerical form. Therefore, the precise simulated impedance bandwidth and fractional bandwidth cannot be reported from the available text alone. These values should be read from the original HFSS data and tabulated in a final journal submission.

5.4 Simulated VSWR

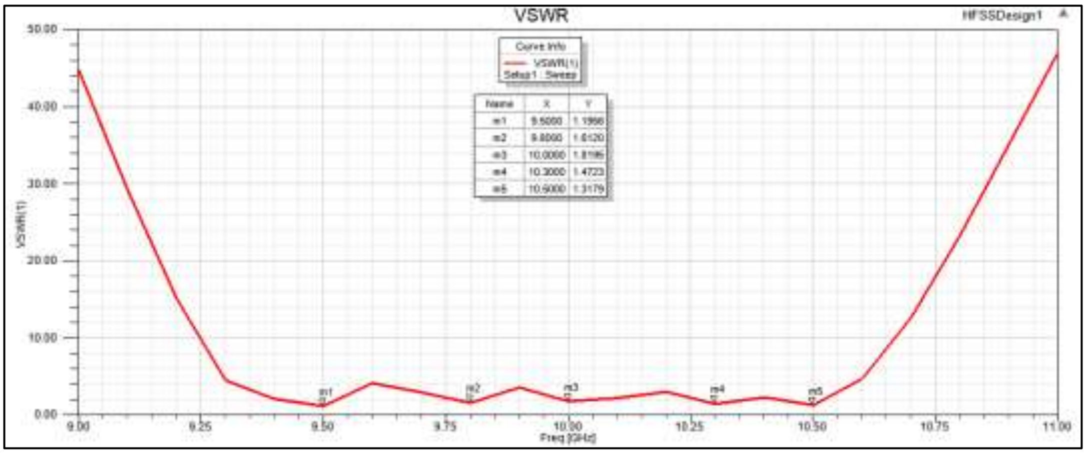

Fig. 9. HFSS-simulated VSWR response of the vertically polarized array

The VSWR plot provides a second representation of the input match. A low VSWR indicates that a large fraction of the incident power is accepted by the antenna rather than reflected back toward the source. The measured and simulated VSWR curves are especially useful when evaluating the effect of the copper-stub tuning described later. The source figure shows a broad low-VSWR region across the intended band, but exact numerical limits should be reported from the underlying data rather than estimated from the rasterized graph.

Table III. Reported Simulated Performance

Performance Metric	Reported Result	Comment
Peak gain	≈ 19 dBi	Obtained from HFSS 3D gain plot
HPBW	≈ 18°	Reported from 2D radiation pattern
Sidelobe level	≈ −12 dB relative to main beam	Reported as "12 dB down"
Beam tilt	≈ 20°	Fixed passive beam tilt
S11	Matched in required band	Exact −10 dB bandwidth not numerically provided
VSWR	Low in required band	Exact band-edge values not numerically provided

6. FABRICATION, TUNING, AND MEASUREMENT

6.1 Prototype Fabrication

After completion of the HFSS design, the array was fabricated on the selected Rogers 5880 laminate. The fabricated board reproduces the four series-fed branches, tapered patch geometry, lower divider network, and coaxial input connection. Hardware fabrication is important because the electrical lengths at 10 GHz are small; dimensional tolerances that appear minor in millimeters can produce measurable phase and impedance changes at X-band.

6.2 Vector Network Analyzer Measurement

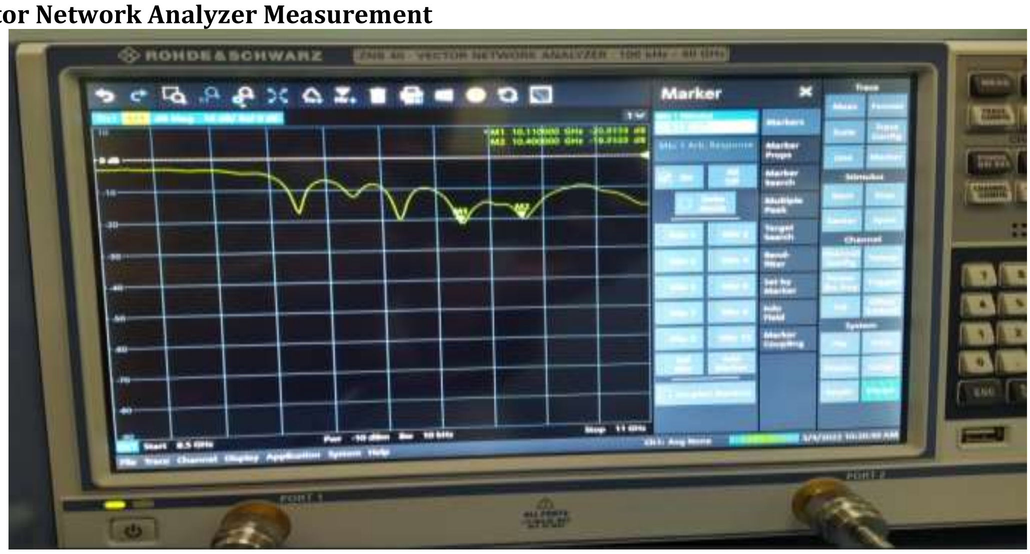

Fig. 10. Practical measured S11 response after post-fabrication tuning.

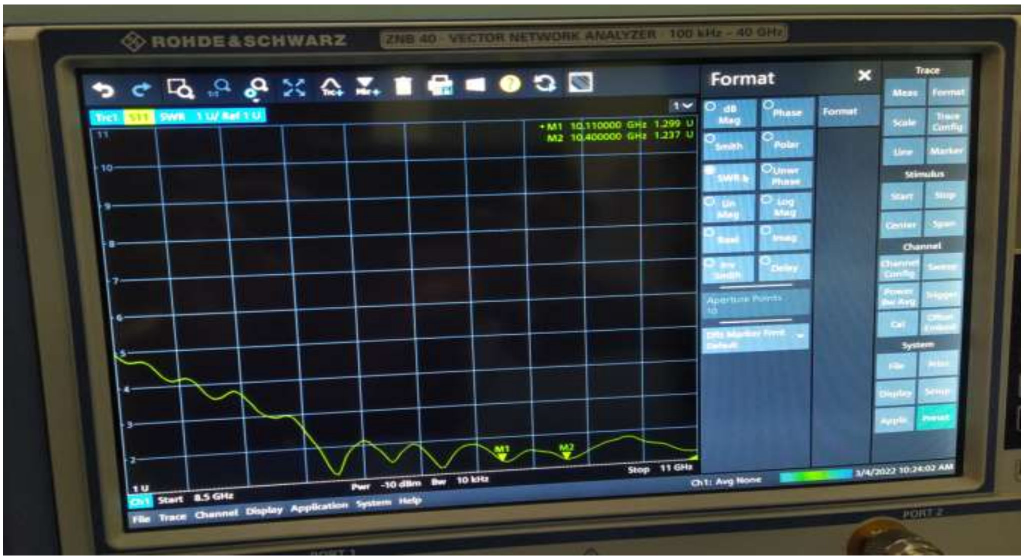

Fig. 11. Practical measured VSWR response after tuning.

The fabricated antenna was measured using a VNA to determine S11 and VSWR. The source manuscript states that the measured matching performance improved after small copper tuning stubs were added to the printed divider tracks. Such tuning changes the local reactive loading and effective electrical length of the feed network, allowing small fabrication-induced deviations to be compensated without redesigning the entire PCB.

The source originally described the tuning objective as keeping the return loss “greater than −10 dB.” To avoid sign ambiguity, the present paper uses the conventional S-parameter statement S11 ≤ −10 dB, or equivalently return loss ≥ 10 dB. The measured plots should ideally be exported directly from the VNA as numerical traces so that resonant frequency, −10 dB bandwidth, minimum S11, and VSWR at 10 GHz can be compared quantitatively with the HFSS values.

6.3 Anechoic-Chamber Arrangement

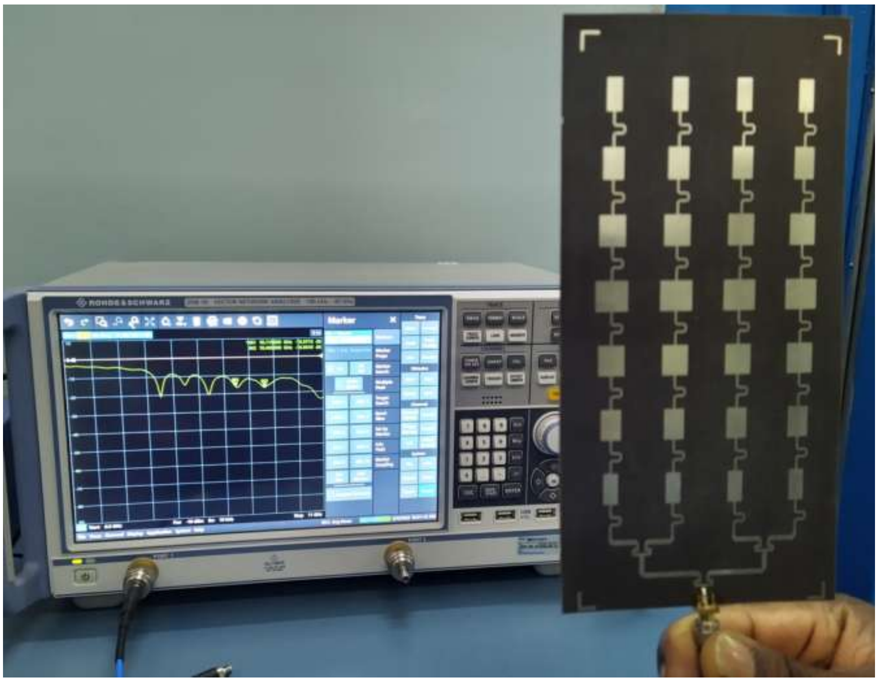

Fig. 12. Fabricated antenna during laboratory measurement with the VNA.

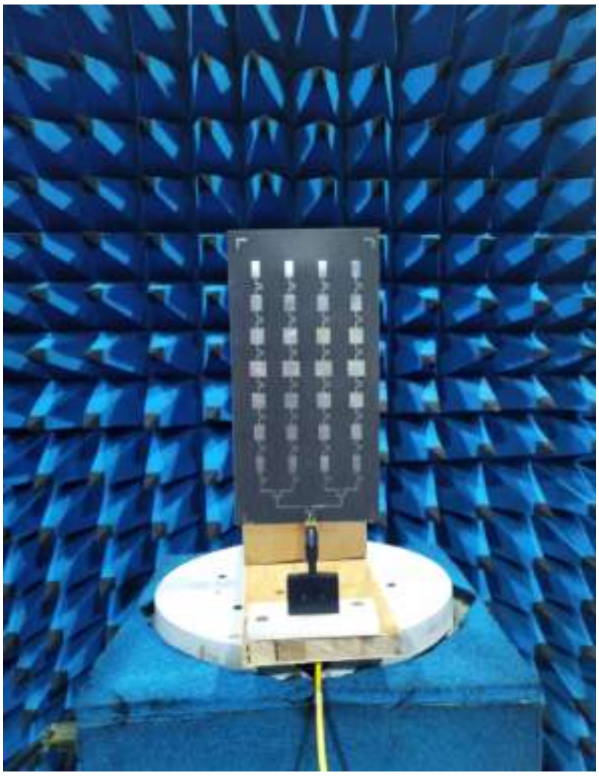

Fig. 13. Antenna mounted inside the anechoic-chamber measurement facility.

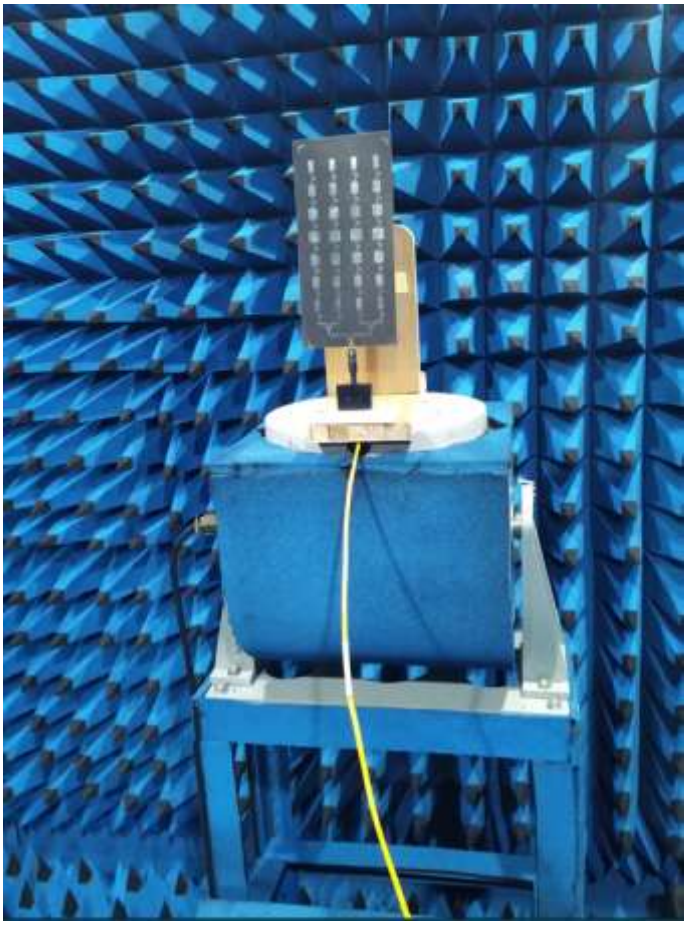

Fig. 14. Additional view of the antenna mounting arrangement in the anechoic chamber.

Fig. 15. Anechoic-chamber range used for the radiation measurement.

Radiation characterization was performed in an anechoic chamber. The chamber absorber suppresses reflections from the walls and surrounding environment, allowing the directional characteristics of the antenna to be measured under conditions that approximate free-space propagation. The source photographs show the array mounted on a fixture and aligned toward the remote measurement antenna.

The source manuscript reports that the practical gain and simulated gain agree within approximately 0.5–1 dB throughout the operational band. This is an encouraging result because a modest difference between simulation and measurement is expected due to connector loss, cable loss, substrate-property tolerance, conductor roughness, finite fixture effects, fabrication tolerances, and calibration uncertainty. However, the source does not include the numerical gain-versus-frequency dataset or overlaid measured and simulated radiation-pattern curves. Those plots should be added to support the stated level of agreement quantitatively.

Table IV. Simulation–Measurement Validation Status

Quantity	Simulation Evidence	Measurement Evidence	Current Reporting Status
S11	HFSS curve provided	VNA curve provided	Qualitative agreement shown; exact bandwidth values not tabulated
VSWR	HFSS curve provided	VNA curve provided	Qualitative agreement shown; exact values not tabulated
Peak gain	≈ 19 dBi reported	Measured gain stated to be within 0.5–1 dB	Measured gain curve/data not included in source
HPBW	≈ 18° reported	Anechoic chamber used	Measured HPBW value not explicitly reported
Sidelobe level	≈ −12 dB reported	Anechoic chamber used	Measured SLL not explicitly reported
Beam tilt	≈ 20° reported	Anechoic chamber used	Measured beam-angle value not explicitly tabulated
Radiation efficiency	Not reported	Not reported	Additional measurement/simulation reporting required
Cross-polarization	Not reported	Not reported	Additional measurement required for a complete antenna characterization

7. PHASE PROGRESSION AND FIXED BEAM TILT

7.1 Array Phase Relationship

The beam direction of an array depends on the relative phase between adjacent elements. For a linear sequence of radiators separated by a distance d, the progressive phase associated with a beam angle θ can be represented by

$$\Delta\varphi = (2\pi d/\lambda_0)\sin\theta \tag{12}$$

where λ0 is the free-space wavelength. The expression provides a useful reference for understanding how geometric spacing and electrical phase determine the direction in which the element fields add coherently.

7.2 Corrected 10 GHz Example

At 10 GHz, the correct free-space wavelength is

$$\lambda_0 = c/f = (3 \times 10^8)/(10 \times 10^9) = 0.03 \text{ m} = 30 \text{ mm} \tag{13}$$

For an illustrative spacing of d = 15 mm = λ0/2 and an angle θ = 30°, the progressive phase is

$$\Delta\varphi = 2\pi(0.015/0.03)\sin 30° = \pi/2 = 90° \tag{14}$$

This example replaces inconsistent wavelength and distance substitutions in the earlier draft. It is included only to demonstrate the phase relationship. The actual phase progression of the fabricated array should be calculated from the implemented guided line lengths and effective dielectric constant, because the series-feed sections are printed on a dielectric substrate rather than operating in free space.

7.3 Interpretation of the Reported 20° Beam Tilt

The reported 20° beam tilt is best interpreted as a fixed property of the passive feed geometry. Each series-fed patch receives a signal whose amplitude and phase have been modified by the preceding line sections and radiating elements. When the accumulated phase progression differs from the broadside condition, the far-field maximum shifts away from 0°. Because the reported hardware does not include phase shifters, PIN diodes, varactors, MEMS switches, or other tuning devices, the demonstrated structure should not be described as electronically beam-steerable or reconfigurable.

8. Discussion

8.1 Gain and Aperture Performance

The approximately 19 dBi simulated gain demonstrates that the 28-element printed aperture provides a substantial gain increase over an individual patch. The corrected idealized array estimate of 20.47 dBi provides a useful upper-level reference rather than an expected exact result. The roughly 1.5 dB difference between the ideal estimate and the HFSS result can arise naturally from tapering, mismatch, coupling, feed loss, and finite efficiency. Therefore, the simulated value is not inconsistent with the element-count estimate.

8.2 Beamwidth, Sidelobes, and Tapering

The reported 18° HPBW is consistent with a directional array whose effective aperture is significantly larger than one wavelength. The sidelobe level of approximately −12 dB indicates that the aperture distribution provides some suppression relative to a strongly uniform excitation. To substantiate the claim of sidelobe suppression by tapering, a stronger paper would compare the proposed tapered geometry with an otherwise identical untapered reference array. Such an ablation would show whether the improvement is caused by the taper rather than by another aspect of the feed or geometry.

8.3 Impedance Matching and Practical Tuning

The need for copper-stub tuning is a practical and informative result. At X-band, the effective electrical length of a printed line is highly sensitive to small dimensional variations. Connector launch geometry and etching tolerances can also change the local impedance. The measured improvement after adding copper stubs shows that the feed-divider section provides a practical location for final impedance correction. For production hardware, the tuned dimensions should be incorporated into the final artwork and re-simulated rather than depending on manual post-fabrication modification.

8.4 Relevance to Radar Applications

The combination of approximately 19 dBi gain, narrow beamwidth, a fixed off-boresight main lobe, and a low-profile printed form factor makes the design relevant to fixed-sector radar and target-tracking installations where a predetermined look angle is acceptable. A fixed beam can reduce RF complexity compared with electronically scanned arrays. If dynamic steering is required, however, the present passive geometry would need to be extended with a controllable phase-shifting or switching network.

9. Limitations And Recommended Additions For Journal Submission

The available simulation and measurement results demonstrate a working antenna prototype, but several items are not numerically documented in the source manuscript. These omissions should be addressed before submission to a selective antenna or microwave journal. The following additions would materially strengthen the paper:

- Report the exact simulated and measured −10 dB impedance bandwidth in GHz and the corresponding fractional bandwidth in percent.
- Provide the minimum simulated and measured S11 values and the VSWR specifically at 10 GHz.
- Export a measured gain-versus-frequency plot and overlay it with the HFSS gain curve.
- Provide overlaid simulated and measured E-plane and H-plane radiation patterns at 10 GHz and, preferably, at the lower and upper band edges.
- Tabulate measured HPBW, beam direction, sidelobe level, front-to-back ratio, and cross-polarization.
- Report simulated radiation efficiency and, if available, measured total efficiency.
- Provide a complete table of all patch dimensions, feed-line widths, line lengths, inter-element spacings, and taper values.
- Document the HFSS port type, boundary conditions, air-box size, adaptive meshing settings, convergence criterion, and frequency sweep.
- Compare the tapered design with an untapered 4 × 7 reference to demonstrate the claimed sidelobe suppression and bandwidth improvement.
- Add a literature-comparison table containing recent X-band printed arrays with columns for element count, substrate, gain, bandwidth, SLL, HPBW, dimensions, and measured status.
- If "conformal" is to be restored to the title, provide curved-structure simulations and measurements for defined bending radii; otherwise retain a planar-array title.
- If a 50–100 W peak-power claim is retained, support it with transmission-line current/voltage limits, thermal analysis, or controlled high-power testing.

10. Conclusion

A detailed analysis of a 10 GHz X-band 4 × 7 tapered series-fed microstrip patch array has been presented. The antenna contains 28 vertically polarized radiating elements implemented on 0.8 mm Rogers RT/duroid 5880 with $\varepsilon_r = 2.2$. Four series-fed branches are driven through a printed input-divider network, and the patch geometry is tapered to shape the aperture distribution. The complete structure was modeled in Ansys HFSS, fabricated, tuned, and experimentally evaluated using VNA and anechoic-chamber measurements.

The reported HFSS results show a peak gain of approximately 19 dBi, an HPBW of approximately 18°, a sidelobe level about 12 dB below the main beam, and a fixed beam tilt of approximately 20°. The measured S11 and VSWR follow the simulated response after copper-stub tuning of the feed-divider tracks. Chamber testing is reported to show measured gain within approximately 0.5–1 dB of simulation across the operational band. The corrected 10 GHz wavelength and array-gain calculations further clarify the relationship between the physical geometry and the reported performance.

Within the evidence provided by the source manuscript, the design is best described as a planar, vertically polarized, fixed-beam X-band array rather than as a demonstrated conformal or electronically reconfigurable antenna. The prototype nevertheless provides a useful experimental basis for a compact radar-array design. With complete quantitative bandwidth data, measured radiation patterns, efficiency results, full geometry disclosure, and a direct comparison against an untapered reference, the work can be developed into a substantially stronger journal manuscript.

References

[1]. R. Y. Hermansyah, F. Y. Zulkifli, and E. T. Rahardjo, "Radiation Characteristics of Slotted Waveguide Array Antenna for X-Band Dual-Polarized Weather Radar," Progress in Electromagnetics Research Symposium (PIERS), Shanghai, China, 8–11 Aug. 2016.

[2]. X. Liu, S. He, H. Zhou, J. Xie, and H. Wang, "A Novel Low-Profile Dual-Band Dual-Polarization Broadband Array Antenna for 2G/3G Basestation," IET International Conference on Wireless, Mobile and Multimedia Networks (ICWMMN), Hangzhou, China, 2006, pp. 1–4.

[3]. C. H. Tsao, Y. M. Hwang, F. Killburg, and F. Dieirich, "Aperture Coupled Microstrip Antenna for Dual or Circular Polarization Capabilities," IEEE AP-S Symposium Digest, 1988, pp. 936–939.

[4]. L. L. Shafai, W. A. Chamma, et al., "Dual-Band Dual-Polarized Perforated Microstrip Antennas for SAR Applications," IEEE Transactions on Antennas and Propagation, vol. 48, no. 1, pp. 58–66, 2000.

[5]. K. Wincza, S. Gruszczynski, and J. Grzegorz, "Integrated Dual-Band Dual-Polarized Antenna Element for SAR Applications," IEEE Wireless and Microwave Technology Conference (WAMICON), Clearwater, FL, USA, Apr. 2009, pp. 1–4.

[6]. G. Jaworski, T. Maleszka, et al., "Dual Frequency and Dual-Linear Polarization Integrated Antenna Array for Application in Synthetic Aperture Radar," European Microwave Conference (EuMC), Paris, France, Sep. 2010, pp. 1714–1717.

[7]. S. H. Hsu, Y. J. Ren, and K. Chang, "A Dual-Polarized Planar-Array Antenna for S-Band and X-Band Airborne Applications," IEEE Transactions on Antennas and Propagation, vol. 51, no. 4, pp. 70–78, 2009.

[8]. G. Vetharatnam, C. B. Kuan, and C. H. Teik, “Combined Feed Network for a Shared-Aperture Dual-Band Dual-Polarized Array,” IEEE Antennas and Wireless Propagation Letters, vol. 4, pp. 297–299, 2005.

[9]. A. Vallecchi, G. B. Gentili, and M. Calamia, “Dual-Band Dual-Polarization Microstrip Antenna,” IEEE Antennas and Propagation Society International Symposium, vol. 4, Columbus, OH, USA, Jun. 2003, pp. 134–137.

[10]. R. B. Waterhouse, “Design of Probe-Fed Stacked Patches,” IEEE Transactions on Antennas and Propagation, vol. 47, no. 12, pp. 1780–1784, 1999.

[11]. Kotla, R. W., Yarlagadda, S. R., Mannala, K., Sreek, D., & Sivarathri, V. M. (2025). Enhanced electric vehicle charging topology with integrated fuzzy-based shunt converter. Acta Polytechnica, 65(3), 296–305. https://doi.org/10.14311/AP.2025.65.0296

[12]. J. Granholm and K. Woelders, “Dual Polarization Stacked Microstrip Patch Antenna Array with Very Low Cross-Polarization,” IEEE Transactions on Antennas and Propagation, vol. 49, no. 10, pp. 1393–1402, 2001.

[13]. Kotla, R. W., Yarlagadda, S. R., and Sarada Devi, T. S. N. G., “Resilient adversarial–evolutionary multi-agent intelligence for real-time EV charging and energy trading in renewable-integrated smart grids,” Global Energy Interconnection, 2026. https://doi.org/10.1016/j.gloei.2025.12.005

[14]. A. U. Zaman, L. Manholm, and A. Derneryd, “Dual Polarized Microstrip Patch Antenna with High Port Isolation,” Electronics Letters, vol. 43, no. 10, pp. 551–552, May 2007.

[15]. Kotla, R. W., Anil, N., Lagudu, J., et al. “Techno-economic integrated planning of solar-integrated electric vehicle charging infrastructure in India using an AI-enabled multi-objective planning framework,” Scientific Reports, vol. 16, p. 6393, 2026. https://doi.org/10.1038/s41598-026-37080-2

[16]. K. S. Kona and Y. R. Samii, “Novel Probe-Feeding Architectures for Stacked Microstrip Patch Antennas,” Microwave and Optical Technology Letters, vol. 38, no. 6, pp. 467–475, Sep. 2003.

[17]. R. W. Kotla, T. S. N. G. Sarada Devi, N. Anil, et al., “Integrated Solar PV Energy Management and Adaptive Control of IPMSM Drives for Lightweight Electric Trikes,” Scientific Reports, 2026, doi: 10.1038/s41598-026-64840-x.

[18]. T. Chan and Y. Hwang, “A Dual-Band Series Feed Microstrip Array Antenna at 10 GHz,” Antennas and Propagation Society International Symposium, Newport Beach, CA, USA, vol. 4, pp. 2132–2135, 1995.

[19]. R. W. Kotla, S. Jadapalli, S. V. Madhavi, et al., “Digital-Twin-Enabled Reinforcement Learning for Energy-Efficient and Reliability-Aware Software-Defined Electric Vehicles,” Scientific Reports, 2026, doi: 10.1038/s41598-026-66331-5.

[20]. Anim K, Danuor P, Park S-O, Jung Y-B. High-Efficiency Broadband Planar Array Antenna with Suspended Microstrip Slab for X-Band SAR Onboard Small Satellites. Sensors. 2022; 22(1):252. https://doi.org/10.3390/s22010252

[21]. T. S. N. G. Sarada Devi, R. W. Kotla, E. Venkatesh, T. Srinivas, B. Kavya, and C. Sairam, “Self-Balancing Thirteen-Level Switched Capacitor Inverter with Multi-Carrier-Based Phase Disposition PWM Control Scheme,” in Power Engineering and Intelligent Systems. PEIS 2025, Lecture Notes in Electrical Engineering, vol. 1461, Springer, 2026, pp. 345–358, doi: 10.1007/978-981-96-9724-3_26.

[22]. R. W. Kotla and S. R. Yarlagadda, "Modelling and Control of a Three Phase PVGT System," 2020 IEEE India Council International Subsections Conference (INDISCON), Visakhapatnam, India, 2020, pp. 96-101, doi: 10.1109/INDISCON50162.2020.00031.

[23]. Srikanth, K., Kunta, S., Kotla, R.W. et al. Learning-Assisted Model Reference Adaptive Control of Unified Power Flow Controller for Enhanced Power Quality. J. Inst. Eng. India Ser. B (2026). https://doi.org/10.1007/s40031-026-01313-9

[24]. M. Pehlivan and K. Yegin, "X-Band Low-Probability Intercept Marine Radar Antenna Design With Improved Bandwidth and High Isolation," in IEEE Transactions on Antennas and Propagation, vol. 69, no. 12, pp. 8949-8954, Dec. 2021, doi: 10.1109/TAP.2021.3096952.

[25]. Wilson, K. R., and Y. Srinivasa Rao. “Effects of partial shading on different structures of solar photovoltaic arrays.” Journal of Mechanics of Continua and Mathathematical Sciences 14. 6 (2019): 845–854.

[26]. K. Kaboutari, A. Zabihi, B. Virdee, and M. P. Salmasi, “Microstrip Patch Antenna Array with Cosecant-Squared Radiation Pattern Profile,” AEU – International Journal of Electronics and Communications, vol. 106, pp. 82–88, 2019, doi: 10.1016/j.aeue.2019.05.003.

[27]. K. R. Wilson and Y. S. Rao, "Comparative Analysis of MPPTT Algorithms for PV Grid Tied Systems: A Review," 2019 2nd International Conference on Intelligent Computing, Instrumentation and Control Technologies (ICICICT), Kannur, India, 2019, pp. 1105-1110, doi: 10.1109/ICICICT46008.2019.8993148.

[28]. Tan Q, Fan K, Yang W, Luo G. Low Sidelobe Series-Fed Patch Planar Array with AMC Structure to Suppress Parasitic Radiation. Remote Sensing. 2022; 14(15):3597.

https://doi.org/10.3390/rs14153597
[29]. W. Wu, J. Yin and N. Yuan, "Design of an Efficient X-Band Waveguide-Fed Microstrip Patch Array," in IEEE Transactions on Antennas and Propagation, vol. 55, no. 7, pp. 1933-1939, July 2007, doi: 10.1109/TAP.2007.900171.
[30]. Yi, H., Mu, Y., Han, J. and Li, L. (2022), Improved bandwidth and radiation efficiency of series-fed patch array using cascaded inset-fed mechanism. Electron. Lett., 58: 866-868. https://doi.org/10.1049/ell2.12641
[31]. S. Pravesh, M. K. Nandana, R. Akshaya, and A. C. J. Malathi, "Study and Design of Heart-Shaped Microstrip Patch Antenna for SART Applications," Results in Engineering, vol. 25, p. 103819, 2025, doi: 10.1016/j.rineng.2024.103819.